Published in *J. Phys. Chem. C*, 2016 (DOI: 10.1021/acs.jpcc.6b10033)

Effect of orientation on bulk and surface properties of Sn-doped hematite (α-Fe_2O_3) heteroepitaxial thin film photoanodes

Daniel A. Grave[1], Dino Klotz[1], Asaf Kay[1], Hen Dotan[1], Bhavana Gupta[2], Iris Visoly-Fisher[2] and *Avner Rothschild[1]

[1]Department of Materials Science and Engineering, Technion - Israel Institute of Technology, Haifa, Israel
[2]Department of Solar Energy and Environmental Physics, Swiss Institute for Dryland Environmental and Energy Research, Jacob Blaustein Institutes for Desert Research, Ben-Gurion University of the Negev, Sede Boqer campus, Israel.

*Corresponding author: avner@mt.technion.ac.il

Abstract

The orientation dependence on the photoelectrochemical properties of Sn-doped hematite photoanodes was studied by means of heteroepitaxial film growth. Nb-doped SnO_2 (NTO) was first grown heteroepitaxially on *c*, *a*, *r*, and *m* plane single crystal sapphire substrates in three different orientations. Hematite was then grown in the (001), (110), and (100) orientations on the NTO films. The structural, morphological, optical, and photoelectrochemical properties of the photoelectrodes were studied. The hematite photoanodes possessed high crystallinity and smooth surfaces. Hole scavenger measurements made in H_2O_2-containing electrolyte revealed that the flux of photo-generated holes arriving at the surface was not significantly affected by orientation. Cathodic shifts in the onset potential for water photo-oxidation of up to 170 mV were observed for (110) and (100) oriented hematite photoanodes as compared to (001) oriented films. These results suggest that varying the orientation of heteroepitaxial thin film Sn-doped hematite photoelectrodes primarily affects charge transfer into the electrolyte arising from the surface properties of the different crystal faces rather than affecting hole transport through the bulk under illumination. Electrochemical techniques were then used to probe the existence of surface states which were found to vary with both exposed crystal face as well as foreign dopant inclusion. Kelvin probe force microscopy (KPFM) measurements revealed correlation between the work function of the hematite films (measured in air) and the flat-band and onset potentials for water photo-oxidation (in alkaline aqueous solution).

Keywords: Hematite, (α-Fe_2O_3), photoanode, epitaxial, surface states, orientation

Hematite (α-Fe_2O_3) has received considerable attention as a photoanode material for solar water splitting due to having many attractive properties such as stability in aqueous solution[1,2], suitable bandgap energy[3], and vast abundance[4]. Despite these benefits, the record[5] reported photocurrent for water photo-oxidation is 5.7 mA / cm^2 at the reversible potential of 1.23 V vs. RHE, significantly lower than the theoretical limit[1] of 12.6 mA / cm^2 predicted from its bandgap energy (2.1 eV). The main reason for the limited performance of hematite photoanodes has been attributed to short lifetime[6] of minority charge carriers and low charge carrier mobility[7], resulting in short diffusion length[8] and significant charge recombination. Routes taken by researchers for improving photoanode performance include nanostructuring to reduce the distance needed for minority charge carriers (holes) to reach the electrolyte[9], optical enhancement using specular substrates for resonance absorption in ultrathin compact films[10], and doping to improve the electronic properties[11].

Another potential route for improvement of hematite photoanodes is crystallographic orientational control. Indeed, theoretical work has predicted anisotropic conduction in hematite with up to four orders of magnitude higher conductivity within the basal plane than in directions orthogonal to it.[12] Experimental studies on hematite single crystals have shown approximately one order of magnitude higher electrical conductivity within the basal plane.[13] A few studies have reported improved photoelectrochemical performance for hematite photoanodes possessing (110) preferred orientation for both nanostructured[14] and compact thin film photoanodes[15]. However, when changing deposition conditions to alter the film or nanostructure orientation, significant changes in film morphology, structure, or composition may occur. One way to limit these spurious effects is to use epitaxial films that provide a model framework in which to study orientational dependence. (110) oriented hematite has been grown epitaxially and shown to possess improved photoelectrochemical performance as compared to polycrystalline films.[16] Very recently, Mashiko et al reported significantly improved onset potential for epitaxial undoped *c*-axis (001) hematite films as compared to *m*-axis (100) films.[17] Despite these findings, it is still unclear how orientation affects the photoelectrochemical properties of hematite photoanodes. Since most work has focused on nanostructured photoelectrodes, it is difficult to determine whether the improvements observed in water splitting performance is a result of enhanced bulk properties due to higher conductivity within the basal plane or from surface effects such as improved kinetics or reduced surface recombination.

In this work, we seek to further understand the effect of crystallographic orientation on the photoelectrochemical performance and present the heteroepitaxial growth of (001, *c*-axis), (110, *a*-axis), and (100, *m*-axis) oriented Sn-doped hematite thin film photoanodes. First, Nb-doped SnO_2 (NTO) transparent electrodes were grown heteroepitaxially on sapphire in different orientations by pulsed laser deposition (PLD). The hematite layers were grown subsequently on top of the NTO electrodes (see methods for details). The change in orientation was induced simply by changing the sapphire substrate orientation, allowing for the use of the same deposition conditions for all films. The morphology, crystallography, and optical properties of the films were examined and the effect of orientation on the film properties and photoelectrochemical performance were studied. The use of compact heteroepitaxial thin films provides a model framework from which the effects of the bulk and surface can be deduced.

Results and Discussion

Figure 1 shows the θ-2θ diffraction patterns of the ~90 nm thick hematite films grown on the various sapphire/NTO substrates. For all four films, only one out-of-plane SnO_2 and α-Fe_2O_3 orientation is observed in each pattern. For films grown on *c*, *a*, *r*, and *m*-plane sapphire substrates, the out of plane orientations can be written as $Al_2O_3(001)||SnO_2(100)||Fe_2O_3(001)$, $Al_2O_3(110)||SnO_2(101)||Fe_2O_3(110)$, $Al_2O_3(102)||SnO_2(101)||Fe_2O_3(110)$, and $Al_2O_3(100)||SnO_2(202)||Fe_2O_3(100)$, respectively. The hematite (α-Fe_2O_3) orientation is (110) for both films grown on *a* and *r*-plane sapphire. Therefore, for the remainder of the work we will distinguish between the (110) hematite films as *a*(110) for films grown on *a*-plane sapphire and *r*(110) for films grown on *r*-plane sapphire. The (001) and (100) oriented hematite films grown on *c* and *m* plane sapphire will be referred to as *c*(001) and *m*(100), respectively. The notations are summarized in Table 1.

Table 1. Out-of-plane orientation of Sn-doped hematite photoanodes studied in this work.

Notation	Out-of-plane orientation
c(001)	Al_2O_3(001)||SnO_2(100)||Fe_2O_3(001)
a(110)	Al_2O_3(110)||SnO_2(101)||Fe_2O_3(110)
r(110)	Al_2O_3(102)||SnO_2(101)||Fe_2O_3(110)
m(100)	Al_2O_3(100)||SnO_2(202)||Fe_2O_3(100)

Rocking curve (RC) scans (not shown) of the symmetric reflections were taken for the differently oriented hematite films. The full-width-half-maximum (FWHM) of the RC reflections for the (002), (110), (110), and (200) Bragg reflections of the *c*(001), *a*(110), *r*(110), and *m*(100) hematite films are 0.08, 1.07, 0.78, and 0.64 °, respectively. The rocking curve width is a measure of the misorientation of the domains about the surface normal, suggesting that the *c*(001) oriented films possessed the lowest out-of-plane mosaic spread and best crystallinity of the studied films. Nevertheless, all samples showed good crystallographic quality and a single out-of-plane orientation, allowing for the investigation of orientation dependence and the study of different crystal surfaces.

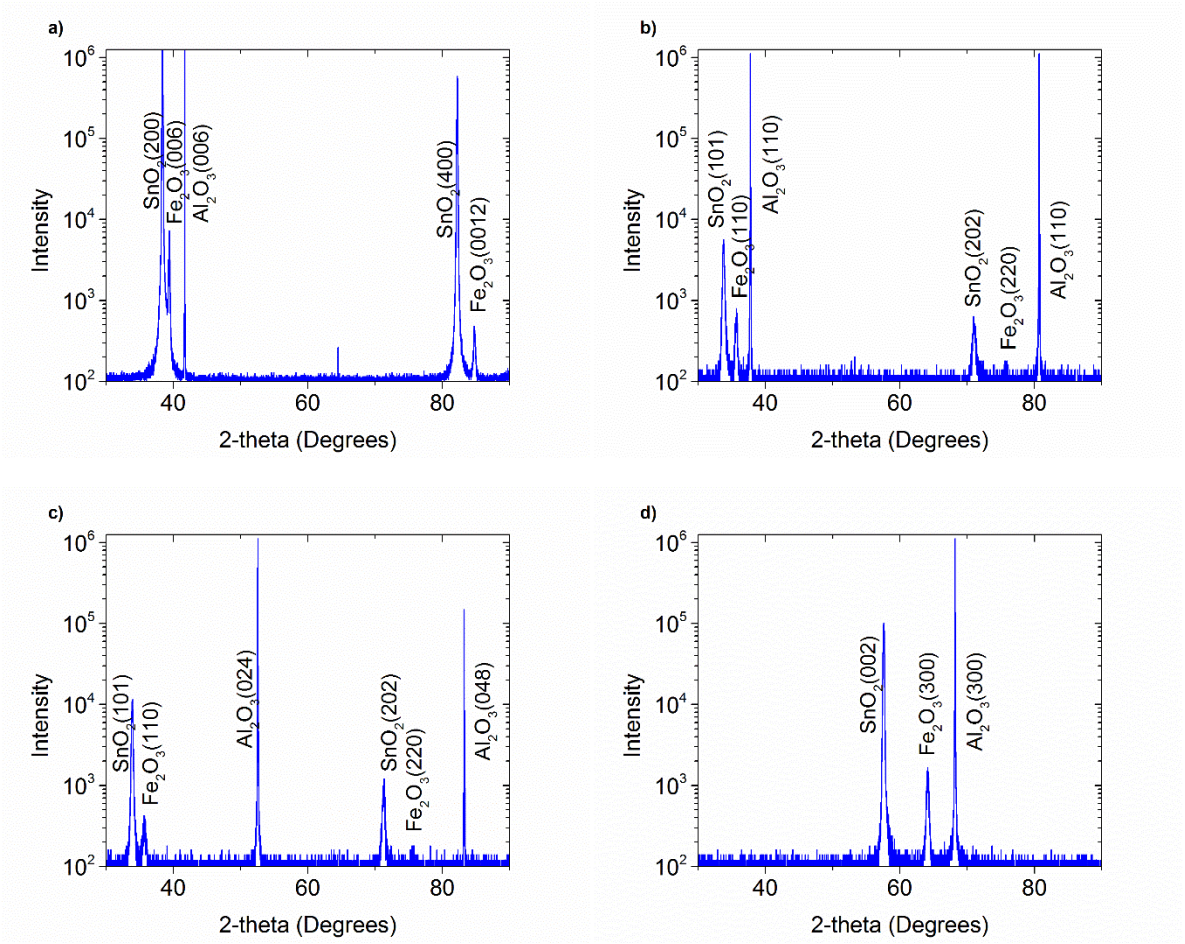

Figure 1. θ-2θ diffraction patterns of ~90 nm Sn-doped hematite films grown on NTO underlayer on (a) *c*-plane, (b) *a*-plane, (c) *r*-plane, and (d) *m*-plane sapphire substrates.

Figure 2 shows the off axis phi scans for all the photoanodes, confirming the heteroepitaxial growth of all measured films. Two rotational domains are observed for *c*(001) hematite whereas fourfold rotational domains are observed for the *m*(100) hematite films. For the films grown on *a*-plane and *r*-plane sapphire which showed the same out of plane alignment, significant difference is observed in the in-plane alignment. Single domain hematite films are observed for the films grown on *r*-plane sapphire, whereas two domains are observed for *a*-plane sapphire. The larger RC peak width for the (110) oriented hematite film grown on *r*-plane versus *a*-plane sapphire may be a result of the twofold domain structure. In all cases, the large (2-3°) FWHM of the peaks in the phi scans suggests the presence of a larger in-plane mosaic spread in these films as compared to heteroepitaxially grown $Al_2O_3(001)||Pt(111)||Fe_2O_3(001)$ films reported elsewhere,[19] which is an indication of larger amounts of extended crystalline defects and low-angle grain boundaries.

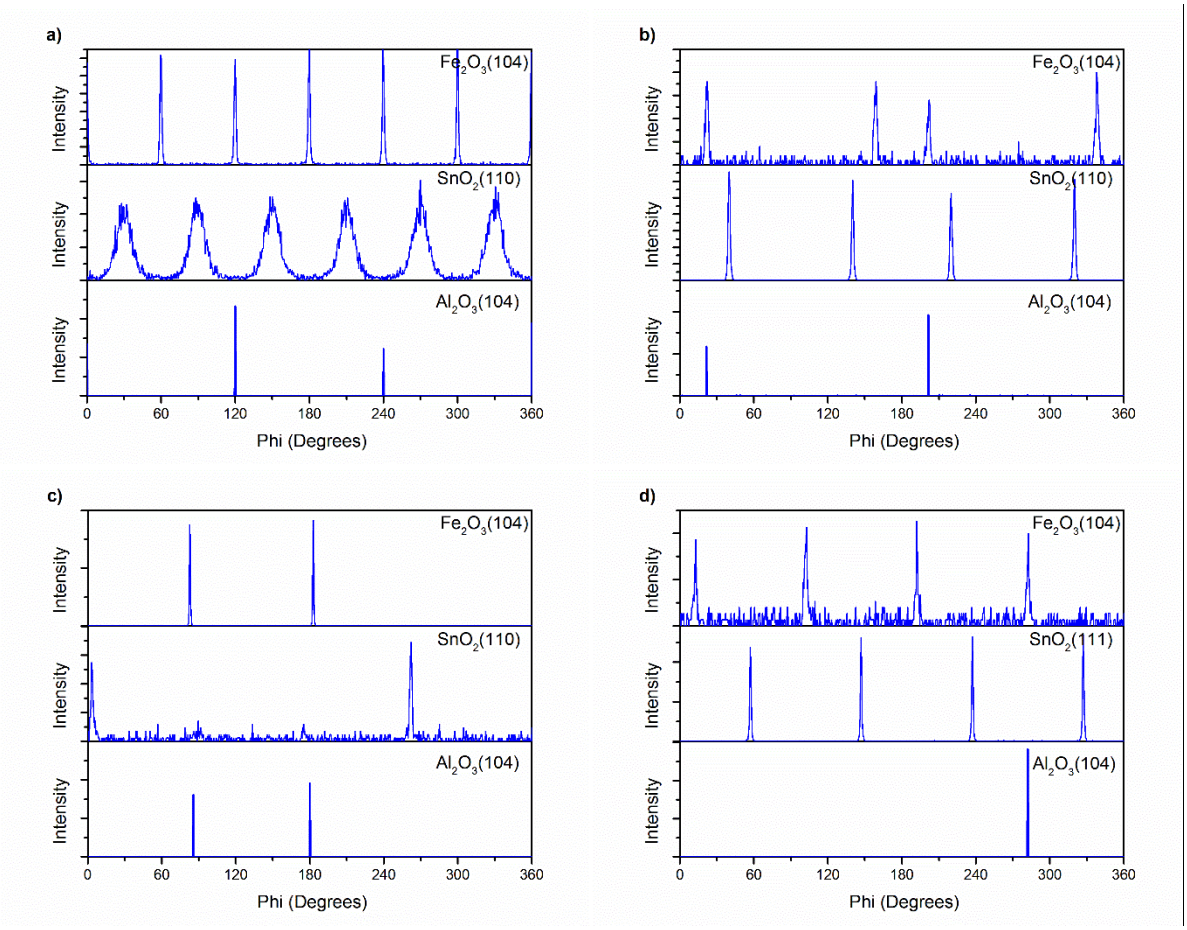

Figure 2. Off-axis phi scans of ~90 nm Sn-doped hematite films grown on NTO underlayer on (a) *c*-plane, (b) *a*-plane, (c) *r*-plane, and (d) *m*-plane sapphire substrates.

Figure 3 shows the AFM images of the various hematite photoanode stacks. The *c*(001) and *m*(100) oriented hematite films show smooth, continuous surfaces with 0.5 and 0.3 nm average roughness, respectively. The two (110) oriented films show rougher surfaces of approximately 2 nm RMS roughness. Before photoelectrochemical investigation, the optical and electrical properties of the different NTO layers were characterized. The measured resistivities by four point probe were 9.9 x 10^{-4}, 1.1 x 10^{-3}, 1.1 x 10^{-3}, 2.2 x 10^{-3} ohms-cm for the NTO films on *c*, *a*, *r*, and *m*-plane sapphire substrates, respectively. The transmittance spectra of the NTO films are shown in Figure 4a. The 70-90% transmittance over the visible spectrum is similar to commercial FTO substrates.[18] The combination of the electrical and optical properties shows that the PLD deposited NTO films are suitable transparent electrodes for hematite PEC devices. The absorptance spectra of the photoanode stacks grown in different orientations were also measured and found to be nearly identical as shown in Figure 4b.

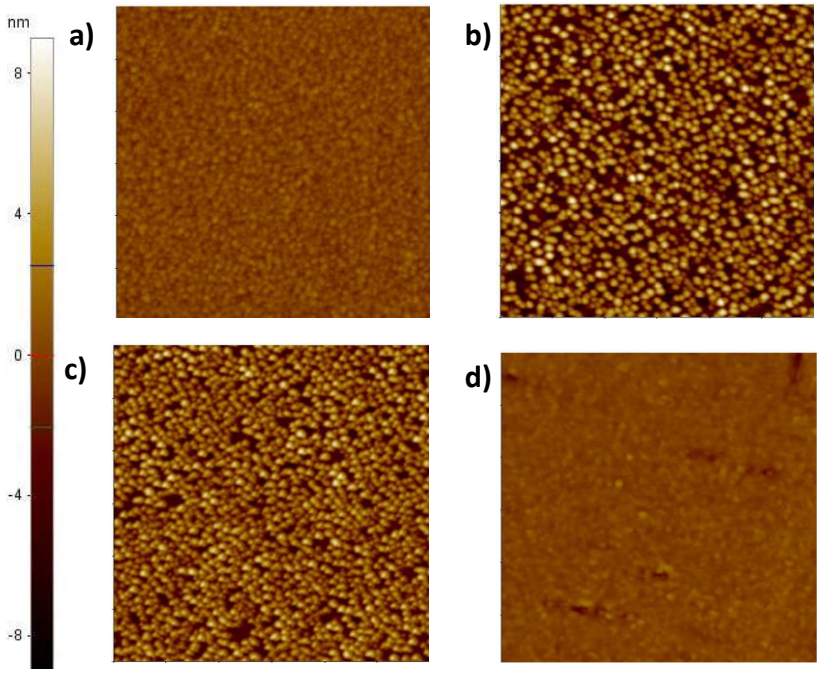

Figure 3. AFM topography of (a) *c*(001) (b) *a*(110) (c) *r*(110), and (d) *m*(100) hematite films. The scan area is 3 x 3 µm.

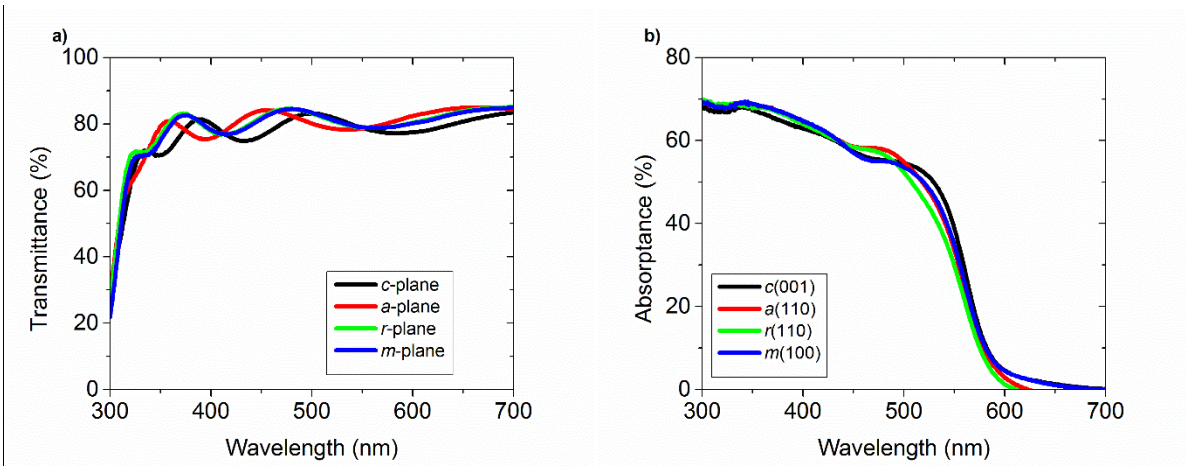

Figure 4. (a) Transmittance spectra of NTO films grown on different sapphire substrates and (b) absorptance of ~90 nm thick Sn-doped hematite films grown on sapphire/NTO substrates.

Photocurrent vs potential (J-U) linear sweep voltammograms measured in 1 M NaOH are shown in Figure 5 for ~90 nm thick Sn-doped hematite films grown in the different orientations. Significant shifts in the onset potential are observed for the differently oriented hematite films with *c*(001) having the worst onset potential. The onset potentials for the *r*(110) and *a*(110) films were shifted cathodically relative to the *c*(001) film by approximately 100 mV while the *m*(100) films exhibited a cathodic shift of approximately 170 mV. All films showed similar photocurrent at high potentials where surface recombination is minimized. J-U curves for the same samples measured in hole scavenger solution of 0.5 M H_2O_2 in 1 M NaOH alkaline solution are shown in Figures 5b. During these measurements, the barrier for charge transfer to the electrolyte is removed and only the bulk-limited hole flux reaching the hematite surface is measured.[20] The H_2O_2 photocurrent is similar for all the films over the measured potential range and consistent with the water photo-oxidation currents measured at high potentials (without H_2O_2).

The photoelectrochemical measurements presented in Fig 5 shed light on the orientation dependence of photoelectrochemical properties in hematite photoanodes. The hole scavenger results suggest that the bulk photocurrent is not largely affected by anisotropy in these devices. Indeed, if charge transport in these films is assumed to proceed through the grain interior along the out-of-plane crystallographic axis, then the reported[13] higher dark conductivity within the basal plane (along *m*[100] or *a*[110] axis) as compared to along the *c*[001] axis does not appear to have significant effect on bulk photocurrent, and instead, the differences observed in the water photo-oxidation performance arise from differences in the surface properties.

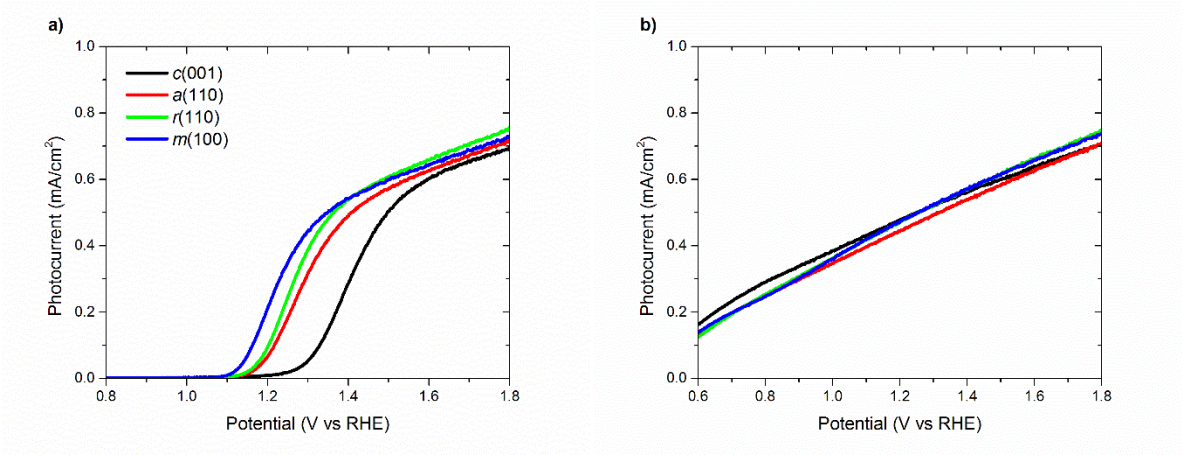

Figure 5. Photocurrent vs. potential (J-U) measurements in (a) 1M NaOH and (b) hole scavenger solution of 1M NaOH + 0.5M H_2O_2 for ~90 nm thick Sn-doped hematite photoanodes.

The onset potentials for water photo-oxidation were extracted by extrapolating the linear part of the J-U voltammograms measured in NaOH to zero and are reported in Figure 6a. The reported results suggest that charge transfer to the electrolyte is significantly affected by the hematite crystal face as demonstrated by the 170 mV cathodic shift in onset potential for films exposing the hematite (100) plane to the electrolyte as compared to those with the (001) basal plane exposed. This is in contrast to what is reported for undoped hematite films deposited on Ta:SnO_2 films where *c*-axis oriented hematite photoanodes showed improved onset potential as compared to *m*-axis oriented samples for thicknesses greater than ~50 nm.[17] For comparison, a thinner Sn-doped hematite film thickness of ~30 nm was also studied and the photoelectrochemical measurements are displayed in Figure S1. Similar trends to the thick films are observed in both water photo-oxidation and hole scavenger measurements for the *c*(001), *a*(110), and *r*(110) samples whereas the *m*(100) samples produce ~20% more photocurrent at high potentials. Measurements made on thinner hematite photoanodes are more prone to surface effects than thicker films and can also be more significantly affected by additional doping and electric fields that arise as the result of the back contact. Therefore, the thicker films give a more accurate representation of bulk transport. Additionally, the difference in onset potential for different orientations with the Sn-doped hematite films reported in this work does not appear to be significantly affected by thickness (seen by comparing Figures 5 and S1) as was reported previously for undoped films.[17] These effects can be explained by the better reproducibility of heavily doped films whose performance is not as susceptible to incorporation of unintentional impurities in the film as compared to undoped films and also to the smaller depletion width due to the high doping level which will result in less interaction with additional space charge arising from the back interface.

To estimate the depletion width values and gain further understanding, capacitance-potential measurements were performed on all the photoanodes in this study (Figure S2a). The extracted flat-band potential and donor density from the Mott-Schottky analyses are shown in Figure 6b and 6c. The extracted donor density is similar for all the samples, showing the benefit of using substrate controlled heteroepitaxial growth where the same deposition parameters can be used to change the growth orientation. For the ~90 nm thick Sn-doped hematite films, the flat-band potential follows similar trend to the onset potential with the *c*(001) film possessing the highest value and the *m*(100) film showing the lowest flat-band potential. A nearly linear correlation is observed (Figure S2b) between the extracted flat-

band potential and the onset potential for water photo-oxidation as has been previously observed for polycrystalline hematite thin films.[21]

The depletion layer widths, W, were calculated using the following formula, $W = ((2\kappa\varepsilon_0 V_{bi})/(qN_d))^{1/2}$ where κ is hematite dielectric constant, ε_0 is the permittivity of free space, V_{bi} is the built-in voltage calculated by subtracting the flat-band potential from the measured potential of 1.23 V vs RHE, q is the elementary charge, and N_d is the donor density. The calculated depletion widths are 5.9, 5.9, 5.9, and 6.5 nm for the *c*(001), *a*(110), *r*(110), and *m*(100) films, respectively. The variations between the samples are small and no direct correlation is observed between the calculated depletion width and photoelectrochemical performance in NaOH or hole scavenger solution. Additionally, the depletion layer widths are significantly smaller than the film thicknesses, which explains the similar trends observed for the thin and thick films.

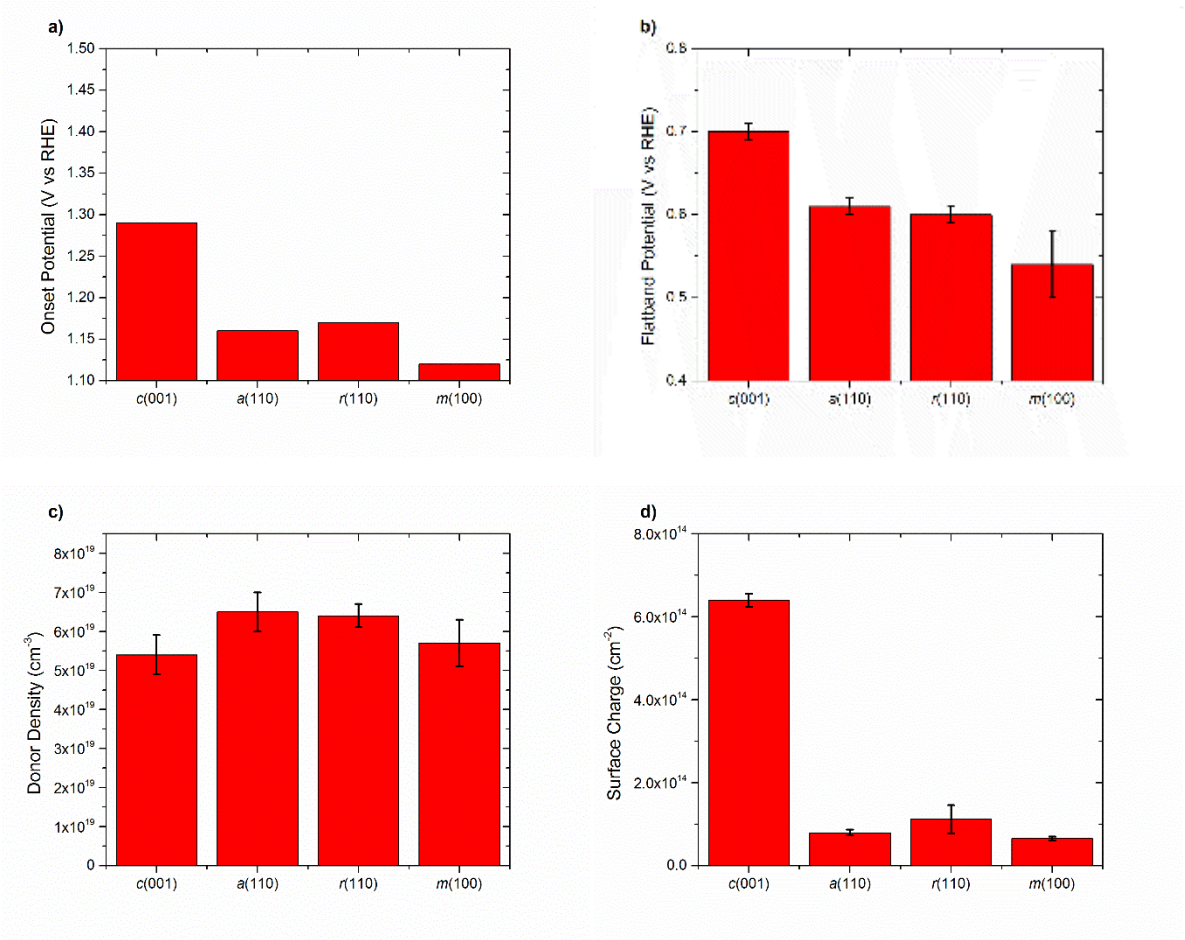

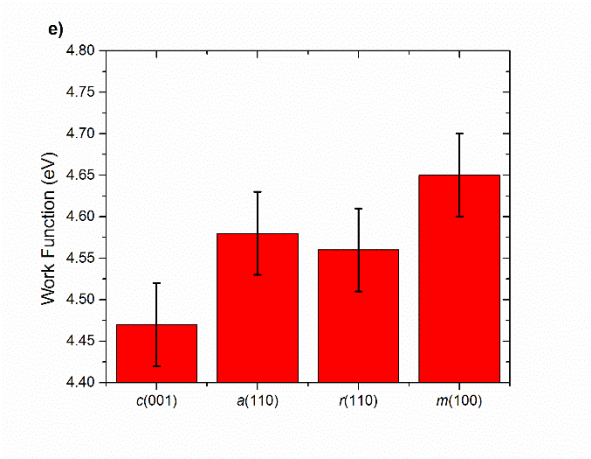

Figure 6. (a) Onset potential, (b) flat-band potential, (c) donor density, (d) surface charge, and (e) work function for the ~90 nm thick Sn-doped hematite films.

To further understand the differences observed in water photo-oxidation performance of the differently oriented hematite samples, we turn our attention to the difference in surface properties between the crystal faces. We employed a technique that was originally used to study surface states in TiO_2 photoanodes[22] and later used to study hematite photoanodes[23,24,25]. For this technique, the photoanodes are pretreated, being held at a constant potential of 2.0 V vs RHE under one sun illumination for 60 s to charge the surface states. Then, the light is promptly switched off and the potential is held for 3 s in the dark before performing 3 cyclic voltammograms from 2.0 to 0.5 V vs RHE at a fixed scan rate. As shown in Figure 7a, where the cyclic voltammograms were measured at a scan rate of 1.5 V/s, the 1st sweep from high to low potential during the 1st scan exhibits a cathodic current in excess to that of the normal dark current that is measured for the remaining scans. The large cathodic current during the 1st sweep of the 1st scan is attributed to the discharging of the previously charged surface states. Therefore, this measurement can be used as a probe to investigate the discharging of the surface states formed during water photo-oxidation. The second sweep (from low to high potential) of the 1st scan and the subsequent 2nd and 3rd scans do not show a cathodic peak indicating a full discharge of the surface states during the 1st scan. The absence of a peak in the anodic direction has been attributed to slow charge transfer and sluggish detrapping, characteristic of a system with high surface recombination.[25] The full measurement was repeated at different scan rates for all the samples. A small negative tail can be observed for the samples at low potentials. Therefore, J measured from the 1st sweep of the 1st scan was subtracted by the 1st sweep of the 3rd scan. The result is called the discharge current, $J_{discharge}$. It is shown in Figure 7b for measurements made with a scan rate of 1.5 V/s on the ~90 nm thick hematite films. Reducing the scan rate results in a decrease of the magnitude of the peak as well as a potential shift towards higher potentials as shown in Fig. S3.

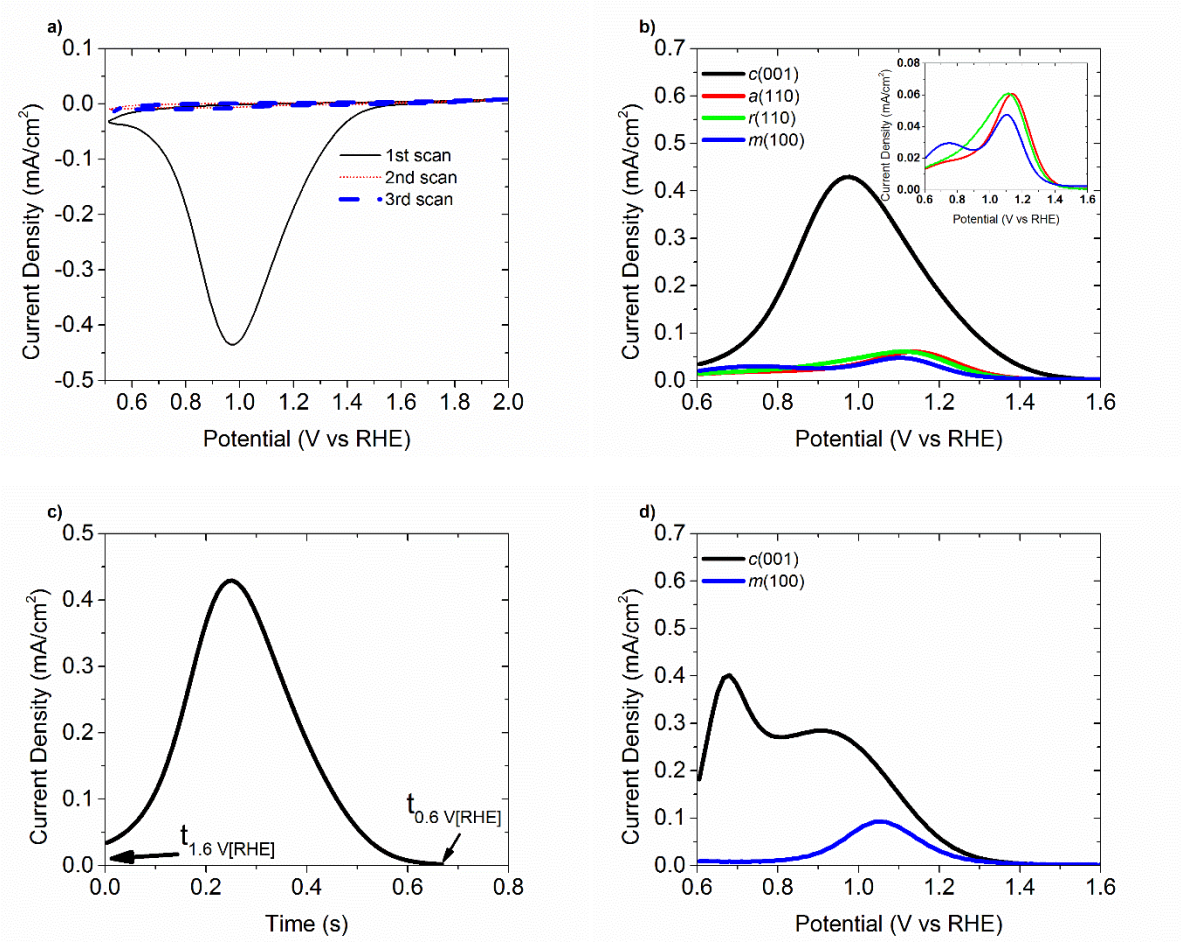

Figure 7. (a) Cyclic voltammetry curves of the ~90 nm thick *c*(001) Sn-doped hematite photoanode after pretreatment. (b) Comparison of the discharge current vs potential for differently oriented Sn-doped hematite photoanodes. (c) Plot of the discharge current vs time for the *c*(001) Sn-doped hematite photoanode. (d) Comparison of the discharge current vs potential for different orientations of undoped hematite photoanodes.

Fig 7c shows the discharge current plotted as a function of time for the *c*(001) data shown in Fig 7b. In order to determine the accumulated surface charge, we integrate the discharge current over time as follows: $Q = \int_{t_{1.6\,V}}^{t_{0.6\,V}} J_{discharge}\, dt$, where $t_{1.6\,V}$ and $t_{0.6\,V}$ are defined as shown in Fig 7c. The value for $t_{0.6\,V}$ will change with scan rate as shown in Fig S4. Figure 6d shows the integrated values for the calculated surface charge. The reported value is an average from the values calculated from the four measurements made at various scan rates for each sample (1.5 V/s, 1 V/s, 800 mV/s, and 400 mV/s). Less than 10% deviation (except for the *r*(110) sample) is observed between the calculated charge for the same sample measured at different scan rates suggesting that the extracted charge is independent of scan rate. Excluding the slowest scan, where the peak is less well defined, the deviation is reduced to less than 5%. Additionally, it is also important to note that the integrated charge density did not change significantly

with film thickness as demonstrated by the similar values for the thinner films (Figure S5), suggesting that this measurement is indeed sensitive to the surface.

Figure 7b compares the experimental data taken at a scan rate of 1.5 V/s from the CV measurements for the various hematite films. The cathodic peak is significantly larger for the *c*(001) film which has the basal plane exposed than for the other samples which have the prismatic (100) and (110) planes exposed and the corresponding integrated charge was nearly one order of magnitude greater for the *c*(001) films. Interestingly, the (110) and (100) films possessed significantly more asymmetric peak profiles than the (001) samples. This is likely due to the existence of two distinct peaks, which is clearly shown in the *m*(100) film. The existence of 2 peaks in polycrystalline hematite films was previously attributed to the existence of two surface states, one of which could be removed with a high temperature anneal, resulting in one peak and improved onset potential.[24]

The differences observed in the CV measurements between the heteroepitaxial hematite films points to the discharging of markedly different surface states during the water photo-oxidation process for different hematite planes. Indeed, these surface species are dependent not only on the orientation of the exposed surface but also on the dopant. Previously, two distinct surface states for undoped *c*-plane hematite films and only one for *m*-plane samples were reported based on impedance spectroscopy results.[17] For comparison, we also prepared undoped hematite films and measured them by the previously mentioned CV method as shown in Figure 7d. Indeed, undoped hematite *c*-plane and *m*-plane samples exhibited two and one cathodic current peaks, respectively, in agreement with those measured by impedance spectroscopy previously. Comparison of Figures 7b and 7d clearly shows that the introduction of the Sn-dopant alters the discharging of the surface states after water photo-oxidation. Therefore, the type and density of the discharged surface states for hematite photoanodes is highly dependent on both the inclusion of a foreign dopant as well as the exposed crystal plane.

The shift in the peak position with scan rate (Figure S3) is due to the scan rate itself and the discharging kinetics of the surface states. The influence of the scan rate can be removed by extrapolating the peak position to indefinitely low scan rates. This allows for estimation of the timescale of the surface discharge processes. The delay time calculated from the peak shifts with respect to zero for infinitely low scan rate is approximately 50 ms for all the measurements. Assuming exponential saturation and the calculated difference as the 3τ value yields a time constant of 17 ms corresponding to a characteristic frequency of 60 Hz for the discharge processes of the surface states, consistent with previous observations made on hematite photoanodes deposited by ALD, as measured with impedance spectroscopy.[23] No significant differences were observed in the timescales of the discharge kinetics for the differently oriented samples.

The integrated charge is well in line with measured charge densities reported in other works on polycrystalline hematite photoanodes.[23,26,27] Considering theoretical hydroxyl site densities[28] of 1.37×10^{15} cm^{-2} for the (001) *c*-plane, and the measured charge of 6.5×10^{14} cm^{-2} extracted from the CV measurement of the *c*(001) film (Fig. 6d), and assuming occupancy of one hole per active site, a surface coverage of approximately 48% is calculated, or approximately one hole per two active sites. The (001) *c*-plane is unique in that it only possesses doubly-coordinated hydroxyl groups.[28] The (100) *m*-plane possesses both singly- and doubly-coordinated hydroxyl groups while the (110) *a*-plane possesses singly, doubly, and triply-coordinated groups.[28] If we assume all groups are active sites and an occupancy of one hole per site, then for the (110) *a*-plane, 1.5×10^{15} cm^{-2} active sites were reported and therefore the calculated surface

coverages are 5 and 7% for the *a*(110) and *r*(110) films. For the (100) *m*-plane with a total site concentration of 8.7×10^{14} cm^{-2}, a surface coverage of 7% is extracted. These coverages are significantly lower than what was measured for the *c*(001) film and can possibly be explained by the existence of singly or triply-coordinated hydroxyl groups on the surface which may affect the charging and discharging kinetics. XPS measurements were performed to probe the hydroxyl content on the surface of hematite films (Fig S6) after being held at constant current of 2.5 mA / cm^2 in the dark in 1 M NaOH solution. In the XPS spectra, the peaks at 530, 531 and 532.5 eV are assigned to oxygen atoms in the lattice (Fe-O lattice), hydroxyl groups in the lattice (Fe-OH lattice), and adsorbed hydroxyl groups (Fe-OH adsorbed), respectively. Consistent with the reported hydroxyl configurations[28], the *c*(001) film was found to have higher Fe–OH lattice content than the *m*(100) film. Additionally, the *c*(001) film was found to have additional –OH adsorbed, also consistent with the higher extracted charge from the CV measurements.

Since the mechanism for water oxidation on hematite surfaces is still under discussion,[27,29,30] it is difficult to assign the importance of the differently coordinated hydroxyl groups to the photoelectrochemical performance. It is interesting to note, however, that the *c*(001) film whose surface contains only doubly-coordinated hydroxyl groups possesses the largest amount of accumulated charges (Fig. 6d) and the highest onset potential for water photo-oxidation (Fig. 6a). This may point towards an enhanced surface recombination facilitated by these ligands or to a larger activation energy for hole transfer. The reduced charging and improved onset potential of the (110) and (100) films could be an indication that water photo-oxidation is assisted by the different hydroxyl configurations on these surfaces. Indeed, it has been found that singly and triply-coordinated groups are less stable and more easily deprotonate than doubly-coordinated groups in aqueous solution.[31] More recently, it has been suggested that the ability of hematite surfaces to dispense with protons appears to play a large role in the kinetics of the oxygen evolution reaction (OER).[32] Nevertheless, many questions still remain open regarding the effect of surface hydroxyl groups on water photo-oxidation. The heteroepitaxial films in this study present a well-controlled model system in which to further explore these surface effects.

The work function of the hematite photoanodes was measured using KPFM. These results are shown in Figure 6e. The measured values are similar to a previously reported value of 4.79 eV for Mn-doped hematite.[33] In the present work, the Sn-doped *c*(001) samples had the smallest work function while the *m*(100) hematite films had the highest work function of the measured samples. Zhu et al. showed that the (001) orientation of undoped hematite was found to possess more negative surface potential (higher work function) than the (110) or (100) orientations.[34] The reasons for the differences in relative changes of the work function between the different orientations may be related to doping and the film fabrication details.

A nearly linear correlation (Figure S7) is observed between the work function and flat-band potential (as well as onset potential) of the hematite photoelectrodes with increasing work function correlating to lower flat-band potential and lower onset potential. Our Sn-doped *c*(001) samples had the smallest work function and worst onset potential while the *m*(100) hematite films had the highest work function of the measured samples and also possessed the lowest onset potential. Zhu et al. found that undoped hematite grains possessing smaller work function resulted in increased reactivity for the reduction of aqueous silver, attributed to more negative band-bending creating a larger built-in field driving electrons to the surface[34]. Mashiko et al. also reported that for water oxidation at high pH, undoped epitaxial hematite photoanodes grown in the *c*(001) orientation showed lower onset potential than films having *m*(100) orientation.[17] The possibility exists that increased positive surface band bending

consistent with higher work function and lower flat-band potential can explain the improved performance of the *m*(100) hematite photoanodes. However, the calculated depletion widths from the Mott Schottky analysis (Fig S2 and discussion above) of the various photoanodes did not scale with photoelectrochemical performance. Therefore, an additional contribution affecting the work function and flat-band potential related to surfaces charges arising from changes in crystalline order at the surface cannot be discounted. Additional work is needed to elucidate these effects and relate them to the photoelectrochemical performance. Nevertheless, we show that bulk transport of photo-generated charge carriers is largely unaffected by orientation, and surface properties control the onset potential of the Sn-doped hematite photoanodes.

Conclusions

The effect of orientation on the photoelectrochemical properties of Sn-doped hematite thin films were studied by means of heteroepitaxial growth on sapphire substrates of different orientations. It was shown that the orientation of the Sn-doped hematite thin film photoanodes primarily affects the surface properties and charge transfer during water photo-oxidation rather than the transport of photo-generated charge carriers through the film. Improvements in onset potential of ~170 mV and ~100 mV were observed for (100) and (110) oriented samples as compared to (001) oriented samples and were found to be correlated with the measured work function and flat-band potential. Additionally, we show that significantly different surface states are probed for different crystal faces and with the introduction of a foreign dopant into the lattice.

Methods

Nb-doped SnO_2 and hematite films were deposited on sapphire *c*, *a*, *m*, and *r*-plane oriented substrates. Prior to deposition, the sapphire wafers were ultrasonically cleaned with soap, acetone, ethanol, and deionized water followed by dipping in Piranha solution (3 H_2SO_4:1 H_2O_2 by volume) and deionized water. The samples were then loaded into the vacuum chamber (PLD/MBE 2100, PVD Products, USA), and pumped to a base pressure of 1×10^{-7} Torr. Nb-doped SnO_2 (NTO) films were deposited by pulsed laser deposition (PLD) from a 1 cation % Nb-doped SnO_2 target. The films were deposited using a PLD system equipped with a KrF (λ = 248 nm) excimer laser (COMPexPro 102, Coherent, GmbH). The NTO films were deposited at a set-point temperature of 800 °C with a laser fluence of approximately 1.1 J / cm^2, repetition rate of 3 Hz, source to substrate distance of 75 mm, and oxygen partial pressure of 5 mTorr. The NTO film thickness was approximately 350 nm. Hematite films were deposited from a 1 cation % Sn-doped Fe_2O_3 target. The hematite films were deposited at a set-point temperature of 800 °C with a laser fluence of approximately 1.1 J / cm^2, repetition rate of 3 Hz, source to substrate distance of 75 mm, and oxygen partial pressure of 10 mTorr. Two hematite film thicknesses were prepared, ~30 and ~90 nm. All characterization discussed in the manuscript refer to the thicker samples unless otherwise noted.

Materials Characterization

The crystalline quality of the films were examined via x-ray diffraction (XRD; Rigaku Smartlab) using Cu K_α radiation, parallel beam optics, and a 2-bounce Ge(220) channel-cut monochromator. All scans were performed after precise alignment of the samples using the sapphire substrate rocking curve scans. High resolution (HRXRD) θ-2θ scans were performed in standard geometry. Off axis phi scans were performed in skew-symmetric geometry to determine the sample in-plane alignment. The surface morphology of the films was characterized by atomic force microscopy (AFM, XE- 100, PSIA Corporation) performed in tapping mode. Scanning Kelvin probe force microscopy (KPFM) was used to calculate the work function of the hematite films using a Keysight 5500 AFM/SPM microscope. Topography images were acquired in tapping mode with App Nano probes coated with Pt. Surface potential measurements and image processing was achieved using WSxM 5.0 software. During measurement, bias was routed to the tip and the contact potential difference (CPD) was calculated using CPD = $\phi_{tip} - \phi_{sample}$. The work function of the tip (ϕ_{tip}) was calibrated with respect to highly oriented pyrolytic graphite (HOPG) so that the work function of the sample could be extracted.

Optical Characterization

The transmittance (*T*) and reflectance (*R*) spectra of the hematite photoanodes were measured using a Perkin Elmer Lambda 950 UV/VIS spectrometer using an integrating sphere accessory. The absorptance (*A*) was calculated for all of the samples as $A = 1 - T - R$. The absorbed photocurrent density, $J_{abs,}$ was then calculated by integrating the spectral irradiance and multiplying it by the absorption spectrum in the wavelength range of 300 to 590 nm according to the formula $J_{abs} = q \int_{300nm}^{590nm} \Phi_{(\lambda)} A_{(\lambda)} d\lambda$ where $\Phi_{(\lambda)}$ is the irradiance spectrum of the light source used for the photoelectrochemical measurements and $A_{(\lambda)}$ is the absorption spectra that was calculated from the spectrophotometer measurements.

Photoelectrochemical characterization

Photoelectrochemical measurements were carried out in "Cappuccino cells" photoelectrochemical test cells[18] connected to a potentiostat (CompactStat, Ivium Technologies). All measurements were carried out in 1 M NaOH aqueous solution (pH = 13.6). The current was measured as a function of the electrode potential using a three-electrode setup with an Ag/AgCl reference electrode and a platinum wire counter electrode. The potential scan rate for the linear sweep voltammograms was 20 mV / s. The applied potential was converted to the reversible hydrogen electrode (RHE) scale using the Nernst equation. The current density was obtained by dividing the measured current by the electrode area immersed in the electrolyte (0.1075 cm^2). This area is also commensurate with the illuminated area of the electrode upon exposure to light. The photocurrent is obtained by subtracting the dark current from the light current (at the same potential). Select measurements were also made in 1 M NaOH + 0.5 M H_2O_2 aqueous solution. A solar simulator (Sun 3000 class AAA solar simulator, ABET Technologies, AM 1.5G) was used for all measurements. Capacitance-potential measurements were performed with the same three-electrode setup described above to obtain Mott-Schottky plots. Measurements were taken at a number of frequencies from 50,000 Hz to 100 Hz and from 1.0 to 1.6 V vs. RHE. The capacitance – potential measurements were carried out in 1 M NaOH + 0.5 M H_2O_2 aqueous solution in order to suppress the parasitic contribution of the surface reaction to the measured capacitance.

Supporting information

Additional chemical and photoelectrochemical characterization of the hematite photoanodes is provided in the supporting information

Author Contributions

The manuscript was written through contributions of all authors. All authors have given approval to the final version of the manuscript

Acknowledgements

This research has received funding from the European Research Council under the European Union's Seventh Framework programme (FP/200702013) / ERC Grant agreement n. [617516]. D. A. Grave acknowledges support by Marie-Sklodowska-Curie Individual Fellowship no. 659491. The results were obtained using central facilities at the Technion's Hydrogen Technologies Research Laboratory (HTRL), supported by the Adelis Foundation, the Nancy & Stephen Grand Technion Energy Program (GTEP) and by the Solar Fuels I-CORE program of the Planning and Budgeting Committee and the Israel Science Foundation (Grant n. 152/11).

References

1. Sivula, K., Le Formal, F. & Grätzel, M. Solar water splitting: progress using hematite (α-Fe(2) O(3)) photoelectrodes. *ChemSusChem* **4,** 432–49 (2011).

2. Dias, P., Vilanova, A., Lopes, T., Andrade, L. & Mendes, A. Extremely Stable Bare Hematite Photoanode for Solar Water Splitting. *Nano Energy* (2016). doi:10.1016/j.nanoen.2016.03.008

3. Gilbert, B., Frandsen, C., Maxey, E. & Sherman, D. Band-gap measurements of bulk and nanoscale hematite by soft x-ray spectroscopy. *Phys. Rev. B* **79,** 035108 (2009).

4. Katz, M. J. *et al.* Toward solar fuels: Water splitting with sunlight and 'rust'? *Coord. Chem. Rev.* **256,** 2521–2529 (2012).

5. Guo, X., Wang, L. & Tan, Y. Hematite nanorods Co-doped with Ru cations with different valence states as high performance photoanodes for water splitting. *Nano Energy* **16,** 320–328 (2015).

6. Joly, A. G. *et al.* Carrier dynamics in α-Fe[sub 2]O[sub 3] (0001) thin films and single crystals probed by femtosecond transient absorption and reflectivity. *J. Appl. Phys.* **99,** 053521 (2006).

7. Morin, F. Electrical Properties of Fe2O3. *Phys. Rev.* **93,** (1954).

8. Kennedy, J. H. & Frese, K. W. Photooxidation of Water at Fe2O3 Electrodes. *J. Electrochem. Soc.* **125,** 709–714 (1978).

9. Warren, S. C. *et al.* Identifying champion nanostructures for solar water-splitting. *Nat. Mater.* **12,** 842–9 (2013).

10. Dotan, H. *et al.* Resonant light trapping in ultrathin films for water splitting. *Nat. Mater.* **12,** 158–64 (2013).

11. Malviya, K. D. *et al.* Systematic comparison of different dopants in thin film hematite (α-Fe_2O_3) photoanodes for solar water splitting. *J. Mater. Chem. A* **4,** 3091–3099 (2016).

12. Iordanova, N., Dupuis, M. & Rosso, K. M. Charge transport in metal oxides: a theoretical study of hematite alpha-Fe2O3. *J. Chem. Phys.* **122,** 144305 (2005).

13. Nakau, T. Electrical Conductivity of α-Fe_2O_3. *J. Phys. Soc. Japan* **15,** 727–727 (1960).

14. Cornuz, M., Grätzel, M. & Sivula, K. Preferential Orientation in Hematite Films for Solar Hydrogen Production via Water Splitting. *Chem. Vap. Depos.* **16,** 291–295 (2010).

15. Kment, S. *et al.* Photoanodes with Fully Controllable Texture: The Enhanced Water Splitting Efficiency of Thin Hematite Films Exhibiting Solely (110) Crystal Orientation. (2015).

16. Seki, M. *et al.* Solid–liquid-type solar cell based on α-Fe_2O_3 heterostructures for solar energy harvesting. *Jpn. J. Appl. Phys.* **53,** 05FA07 (2014).

17. Mashiko, H., Yoshimatsu, K., Oshima, T. & Ohtomo, A. Fabrication and Characterization of Semiconductor Photoelectrodes with Orientation-Controlled α-Fe_2O_3 Thin Films. *J. Phys. Chem. C* **120,** 2747–2752 (2016).

18. Malviya, K. D., Dotan, H., Yoon, K. R., Kim, I.-D. & Rothschild, A. Rigorous substrate cleaning process for reproducible thin film hematite (α-Fe2O3) photoanodes. *J. Mater. Res.* 1–9 (2015). doi:10.1557/jmr.2015.300

19. Grave, D. A. *et al.* Heteroepitaxial hematite photoanodes as a model system for solar water splitting. *J. Mater. Chem. A* (2016). doi:10.1039/C5TA07094E

20. Dotan, H., Sivula, K., Grätzel, M., Rothschild, A. & Warren, S. C. Probing the photoelectrochemical

properties of hematite (α-Fe 2 O 3) electrodes using hydrogen peroxide as a hole scavenger. *Energy Environ. Sci.* **4,** 958–964 (2011).

21. Iandolo, B. *et al.* Correlating flat band and onset potentials for solar water splitting on model hematite photoanodes. *RSC Adv.* **5,** 61021–61030 (2015).

22. Wilson, R. H. Observation and Analysis of Surface States on TiO[sub 2] Electrodes in Aqueous Electrolytes. *J. Electrochem. Soc.* **127,** 228 (1980).

23. Klahr, B. *et al.* Electrochemical and photoelectrochemical investigation of water oxidation with hematite electrodes. *Energy Environ. Sci.* **5,** 7626 (2012).

24. Zandi, O. & Hamann, T. W. Enhanced Water Splitting Efficiency Through Selective Surface State Removal. *J. Phys. Chem. Lett.* **5,** 1522–1526 (2014).

25. Bertoluzzi, L., Badia-Bou, L., Fabregat-Santiago, F., Gimenez, S. & Bisquert, J. Interpretation of Cyclic Voltammetry Measurements of Thin Semiconductor Films for Solar Fuel Applications. *J. Phys. Chem. Lett.* **4,** 1334–1339 (2013).

26. Cummings, C. Y., Marken, F., Peter, L. M., Upul Wijayantha, K. G. & Tahir, A. A. New Insights into Water Splitting at Mesoporous α-Fe $_2$ O $_3$ Films: A Study by Modulated Transmittance and Impedance Spectroscopies. *J. Am. Chem. Soc.* **134,** 1228–1234 (2012).

27. Le Formal, F. *et al.* Rate Law Analysis of Water Oxidation on a Hematite Surface. *J. Am. Chem. Soc.* **137,** 6629–6637 (2015).

28. Barrón, V. & Torrent, J. Surface Hydroxyl Configuration of Various Crystal Faces of Hematite and Goethite. *J. Colloid Interface Sci.* **177,** 407–410 (1996).

29. Yatom, N., Neufeld, O. & Caspary Toroker, M. Toward Settling the Debate on the Role of Fe $_2$ O $_3$ Surface States for Water Splitting. *J. Phys. Chem. C* **119,** 24789–24795 (2015).

30. Zandi, O. & Hamann, T. W. Determination of photoelectrochemical water oxidation intermediates on haematite electrode surfaces using operando infrared spectroscopy. *Nat. Chem.* **8,** 778–783 (2016).

31. Hiemstra, T. & Van Riemsdijk, W. H. Effect of Different Crystal Faces on Experimental Interaction Force and Aggregation of Hematite. *Langmuir* **15,** 8045–8051 (1999).

32. Chatman, S., Zarzycki, P. & Rosso, K. M. Spontaneous Water Oxidation at Hematite (α-Fe $_2$ O $_3$) Crystal Faces. *ACS Appl. Mater. Interfaces* **7,** 1550–1559 (2015).

33. Gurudayal *et al.* Improving the Efficiency of Hematite Nanorods for Photoelectrochemical Water Splitting by Doping with Manganese. *ACS Appl. Mater. Interfaces* **6,** 5852–5859 (2014).

34. Zhu, Y., Schultz, A. M., Rohrer, G. S. & Salvador, P. A. The Orientation Dependence of the Photochemical Activity of α-Fe $_2$ O $_3$. *J. Am. Ceram. Soc.* **99,** 2428–2435 (2016).